

**MODELING, SIMULATION, AND OPTIMIZATION OF A MONOPOD HOPPING ON
YIELDING TERRAIN**

By

Juntao He

Master's thesis

Submitted in Partial Fulfillment of the
Requirements for the Degree of

MASTER OF SCIENCE IN MECHANICAL ENGINEERING

EVANSTON, Illinois

August 2021

ACKNOWLEDGEMENTS

First of all, I would like to thank Prof. Kevin Lynch, Prof. Paul Umbanhowar and Dan Lynch for their invaluable help and support on my master's thesis.

I would also like to thank all the staff at Northwestern University, especially those who fight on the Covid-19 front line. Without them, I could never finish my thesis and course of study in these tough times.

Finally, I would like to thank my parents for their support of my master's study. They are my strong backing in the Covid pandemic.

TABLE OF CONTENTS

Acknowledgments	1
List of Tables	4
List of Figures	5
Chapter 1: Introduction and Background	7
1.1 Chrono simulation environment	7
1.2 Thesis outline	8
Chapter 2: Chrono environment validation	10
2.1 Simulation setup	10
2.2 Comparison between DEM results and experiments	12
2.3 The influence of the intrusion speed on ground reaction force	13
Chapter 3: Ground Reaction Force model	16
3.1 Simulation setup	16
3.2 Resistive forces fitting functions	19
Chapter 4: Periodic Hopping of a Monopod	24
4.1 Soft ground model	25
4.2 Robot model	26

4.3	Robot control	27
4.3.1	Feedforwrđ control	28
4.3.2	Feedforward plus feedback control	30
4.4	Multiple hops	33
Chapter 5: Conclusion		39
References		41

LIST OF TABLES

2.1	Chrono simulation parameters	12
2.2	DEM stress gradient results of three different penetration velocities compared to experiments	15
3.1	Chrono simulation parameters	17
3.2	Coefficients for 2nd order Fourier filtered force functions.	20
4.1	Physical properties of the monopod robot.	26
4.2	Boundary conditions	30

LIST OF FIGURES

2.1	Sketch of a rigid plate intruder	11
2.2	Stress results of three different penetration velocities	14
2.3	Comparison of experimental and DEM results	14
2.4	Normalized error map	15
3.1	Bed cooling graph	18
3.2	Logarithmic bed cooling graph	18
3.3	Raw stress gradient colormaps and their Fourier filtered colormaps	21
3.4	1st order $\alpha_{z,x}$ error maps	21
3.5	2nd order $\alpha_{z,x}$ error maps	21
3.6	3rd order $\alpha_{z,x}$ error maps	22
3.7	Stress gradient error bars	22
4.1	Physical models of the monopod robot and soft ground.	25
4.2	Sketch of phase transitions	28
4.3	Planned single-hop monopod trajectories and their control signals	31
4.4	Block diagram of feedforward plus feedback control for stance phase	33
4.5	CoM trajectories from optimal(desired) and for the two different control strategies	34

4.6	Position and velocity errors of two different control strategies for multiple impact velocities	34
4.7	Experimental errors vs. foot size	35
4.8	Center of mass trajectories for five hops	36
4.9	Error of robot CoM trajectories after five hops for different impact velocities	37
4.10	Screenshot of demo video	38

CHAPTER 1

INTRODUCTION AND BACKGROUND

Mobile robots have great potential to improve search and rescue, disaster response, factory inspection and package delivery. Legged locomotion has significant advantages over wheeled locomotion on yielding surfaces, such as soil, sand, snow and gravel. However, researchers have mainly focussed on generating stable walking and running gaits on rigid flat [1] or uneven terrain [2]. There are far fewer studies about legged locomotion on yielding ground.

Researchers already made robots to accomplish some locomotion tasks on soft ground. Earlier work used fixed kinematics (fixed gaits) to move on soft ground [3] [4]. Only recently has the community started to look at feedforward control [5]. In [5], Hubicki et al. present a model and fast optimization formulation which generates accurate motion plans on granular media with relatively short solving times. Reference [6] achieved flat-footed bipedal walking on deformable granular terrain with feedback control, but they did so by seeking to avoid ground penetration. Reference [7] suggests an active damping controller to reduce the energy cost for monopedal vertical hopping on soft ground, while reference [8] seeks to minimize energy loss on soft-landing using feedforward force control as well as optimal impedance.

In this work, I use feedforward control to develop a periodic gait on soft ground using a ground reaction force model. I test this approach by performing discrete element method (DEM) simulations of the monopod robot hopping on granular materials. To stabilize the target gait, I introduce a feedback term.

1.1 Chrono simulation environment

To test the force control approach I develop for periodic hopping on soft ground, experimental validation using a real robot on real ground would be preferable. However, due to the challenges of working in the lab during the Covid-19 pandemic, I instead chose to validate the control approach

in a virtual environment, namely Chrono. Chrono¹ is a physics engine with specialized support for simulating interaction between rigid bodies and granular media. Chrono supports C++ and Python, but the support for Python is still under construction, so to take full advantage of Chrono's features, C++ is recommended. Chrono's discrete element method (DEM) code works with a GPU but there is no need for users to write GPU code because Chrono's developers already provided libraries for the GPU part. Chrono provides interfaces with CAD programs like SOLIDWORKS to simplify model building in Chrono. Chrono also has better integration of rigid-body dynamics with DEM simulation than other DEM simulators such as LAMMPS² and LIGGGHTS³.

In the following chapters, I use Chrono to generate resistive forces approximation functions of the ground reaction force and test the analytic feedforward force control solution generated by MATLAB using the RFT model. Advantages of the Chrono simulation environment over real world experiments include:

1. To the extent that the DEM simulation is physically accurate, in-simulation validation provides more feedback than hardware validation, since potentially any variable of interest can be measured and recorded. This results in a better-informed motion planning framework.
2. The cost of experimental setup and the cost of experimental failure are both lower than with hardware experiments.
3. The performance of the robot and its control on different soft substrates can be investigated by simply changing the parameters related to the physical properties of the granular materials.

1.2 Thesis outline

The structure of the thesis is as follows:

Chapter 2 validates the reliability and accuracy of the Chrono simulation environment by compar-

¹<http://api.projectchrono.org/5.0.0/>

²<https://lammms.sandia.gov/>

³<https://www.cfdem.com/liggghts-open-source-discrete-element-method-particle-simulation->

ing simulation results with experimental results from Li et al. [3]. Chapter 3 generates functions to predict ground reaction forces from granular media using a Fourier representation matched to Chrono simulation data. Chapter 4 develops a control strategy which enables the 1D hopping monopod to jump back to its original maximum height. Chapter 5 compares the performance of feedforward controls in the DEM simulation for a range of hop heights and for hoppers with different foot areas. Chapter 6 presents the conclusions.

CHAPTER 2

CHRONO ENVIRONMENT VALIDATION

To validate the Chrono simulation environment, I compared my simulation results with the experimental results in Li et al. [3].

Reference [3] finds that the granular resistive stresses are linear with depth, but only for low intrusion speeds (less than 0.5 m/s), only in the bulk, i.e., away from the container sides (to avoid Janssen effects [9]) and at depths both large enough to avoid nonlinearities due to free particles at the surface and small enough to avoid nonlinearities due to compression against the container bottom. For a rigid plate intruder moving in granular media [3], the lithostatic stresses can be modeled as

$$\sigma_{z,x}(|z|, \beta, \gamma) = \begin{cases} \alpha_{z,x}(\beta, \gamma)|z| & z < 0, \\ 0 & z > 0, \end{cases} \quad (2.1)$$

where $\sigma_{z,x}$ are the vertical (z -component) and horizontal (x -component) resistive stresses, z is the depth of the intruder, and $\alpha_{z,x}$ are vertical and horizontal stresses per unit depth in the linear response regime. Note that when the intruder is above the granular domain ($z > 0$), there are no resistive stresses. Angle of attack β and angle of intrusion γ are shown in Figure 2.1.

2.1 Simulation setup

Figure 2.1 shows a planar view of the plate penetrating into the granular domain. The black rectangle represents the plate while the colored area represents the granular media. The plate has dimensions of 3.81 cm \times 2.54 cm \times 0.64 cm (area = 9.68 cm²) and a density of 2.7 g/cm³, which match the dimensions and density of the flat plate used by Li et al. in [3]. All the spheres in the granular domain have identical physical properties, specifically a radius of 3.2 mm and a density of 2.6 g/cm³. The spheres are contained in a box with cross section 24 cm \times 22 cm, and fill the box to a depth of approximately 18 cm. The bed is prepared by filling the container from the bottom to

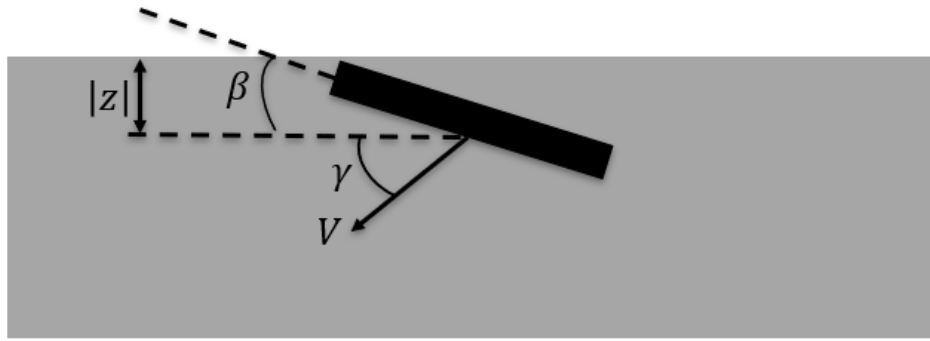


Figure 2.1: The rigid plate intrudes into the granular media with velocity V , attack angle β and intrusion angle γ . The distance between the CoM of the plate and the granular bed top, $|z|$, is the intrusion depth.

the top layer by layer. Li et al. used a few different granular materials in their experiments. I chose 3.2 mm diameter glass spheres instead of those materials with small radius here because I can use far fewer granular spheres for my simulation than smaller radius. This makes our simulation time cost more acceptable. That is, the simulation time for a specific $\gamma - \beta$ pair intrusion trial is 2 to 3 minutes. For materials with larger radii, fewer particles contact a fixed size plate, resulting in larger force fluctuations [10], a topic I return to in the context of feedback control in Chapter 4. Considering both reducing force fluctuations and simulation time, 3.2 mm is a good choice for the granular particle radius. Table 2.1 lists the simulation parameters, for more details, refer to the JSON file in my GitHub repository ¹. The friction is chosen the same as used in [3]. Damping coefficients are not mentioned in [3], I set them as reasonable values for glass.

To reproduce the stress parameters results for 3 mm glass spheres from the experiments shown in Fig. S4(I, J) in the supplementary materials of [3], I did 271 simulations with attack angle β and intrusion angle γ varied from -90 degrees to 90 degrees (three repeated trials for each β and γ pair). For the intrusion speed V , I chose 3 cm/s because it guarantees both accuracy (how close the simulation results are to experimental results in [3]) and time-efficiency. Further discussion of the choice of intrusion speed can be found at the end of this chapter. In each simulation, β and γ are

¹https://github.com/HappyLamb123/Foot-ROBOT/blob/master/demo_code/plate/demo_GRAN_plate.json

Time step	1e-5 s
Plate dimension	3.81 cm \times 2.54 cm \times 0.64 cm
Plate density	2.7 g/cm ³
Sphere radius	3.2 mm
Sphere density	2.6 g/cm ³
Domain size	24 cm \times 22 cm \times 18 cm (depth)
Sphere-sphere normal contact stiffness	1e8 N/m
Sphere-wall normal contact stiffness	1e8 N/m
Sphere-sphere normal damping coefficient	6000 N s/m
Sphere-wall normal damping coefficient	6000 N s/m
Sphere-sphere tangent contact stiffness	1e6 N/m
Sphere-wall tangent contact stiffness	1e6 N/m
Sphere-sphere tangent damping coefficient	0
Sphere-wall tangent damping coefficient	0
Sphere-sphere static friction coefficient	0.63
Sphere-wall static friction coefficient	0.63

Table 2.1: Parameters for Chrono granular simulations.

fixed during penetration and the absolute value of intrusion speed V is 3 cm/s. In the Chrono simulation, I record the horizontal and vertical resistive forces of the granular media every microsecond into a CSV file. Then, I divide the resistive forces by the area of the rigid plate to get the stress in the x - and z - direction. To get the stress gradient, I linearly fit the horizontal and vertical direction stress from 2 cm to 7.5 cm. The resulting slopes of the lines are the stress gradient, $\alpha_{z,x}$. I choose the depth range for fitting in order to avoid surface effects and effects from the container bottom.

2.2 Comparison between DEM results and experiments

As [3] suggests, the stresses in the horizontal and vertical directions are proportional to the penetration depth as Figure 2.2 shows. By linearly fitting the stress versus depth curves in MATLAB, the stress gradients (α_x and α_z) can be calculated as the slopes of those fitted curves. Figure 2.3 shows the Chrono simulation results and experimental results of x and z direction stress gradients for different β and γ . These DEM simulation results show that horizontal and vertical resistive stresses scale linearly with intruder depth, indicating that the DEM simulations are a viable alternative to experiments performed with real granular media. The upper two plots in Figure 2.3 show

experimental results from Li et al., while the lower two are DEM results generated by Chrono. As Figure 2.3 indicates, the simulation results closely match the experimental results. To better characterize the accuracy of the Chrono simulation environment, a normalized error map is presented in Figure 2.4. The normalized errors in Figure 2.4. are calculated as,

$$\varepsilon_i = \frac{\alpha_{i,\text{DEM}} - \alpha_{i,\text{Exp}}}{\bar{\alpha}_{i,\text{Exp}}}, \quad (2.2)$$

where i is x or z , $\alpha_{i,\text{DEM}}$ represents the horizontal (x) or vertical (z) direction stress per cubic centimeter of DEM results while $\alpha_{i,\text{Exp}}$ represents experimental results of Li et al.[3]. The $\bar{\alpha}_{i,\text{Exp}}$ term in the denominator represents the mean value of all the experimental results .

As the color map in Figure 2.3 indicates, the normalized errors are close to zero in most regions of the $\beta - \gamma$ plane. Only a few parts are dark red or blue where the simulation results and experimental results show larger differences. For z -direction normalized errors, the darkest color can be found in the column where $\gamma = 90$ degrees. As for x -direction normalized errors, the darkest color can be found in the columns where γ equals 18.435, 45 and 55.31 degrees. Other regions of the $\beta - \gamma$ plane have very small error values (less than 0.2). So the simulation results have a good match to the experimental results.

2.3 The influence of the intrusion speed on ground reaction force

In my simulations, the intrusion speed is 3 cm/s while Li et al. used 1 cm/s in their experiments. I opted for a faster intrusion speed because the rigid plate can reach the same depth in less time with a higher intrusion speed. A more acceptable time cost can help us to get more datasets in the same time period. For the robot control discussion in Chapter 4, a more efficient simulation time can help reduce the barrier to testing new control policies. With less time spent in simulation, I can iterate faster and converge to an effective control policy sooner. To determine the influence of speed variations, I ran three simulations with different penetration velocities (Figure 2.2). In

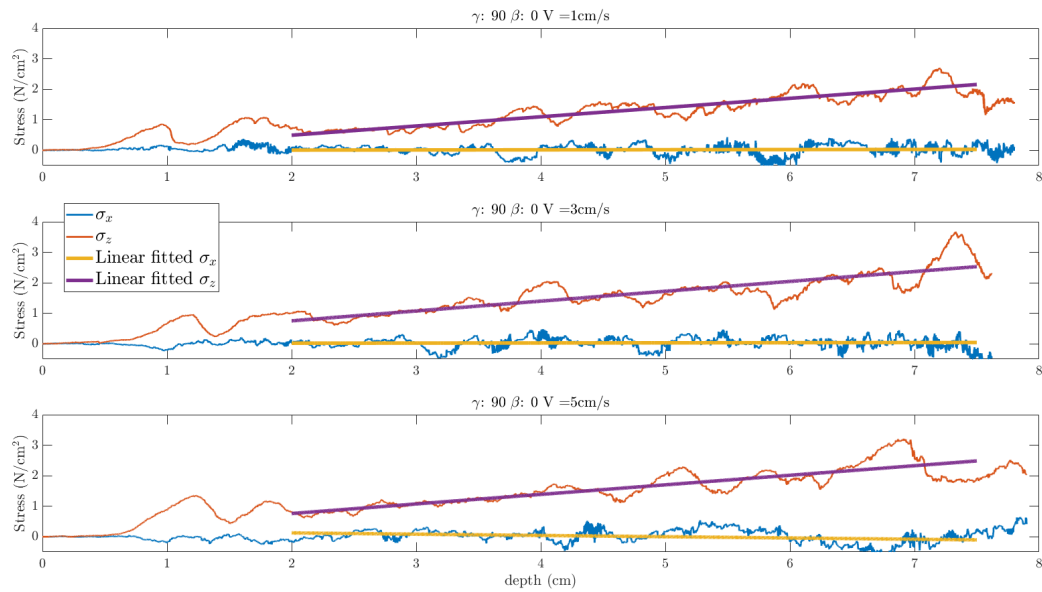


Figure 2.2: Vertical (z) and horizontal (x) stresses vs. penetration depth and corresponding linear fits (lines). Similar results for intrusion velocities of 1, 3, and 5 cm/s indicate that 3 cm/s is a good choice for balancing simulation time and accuracy relative to experimental results in [3].

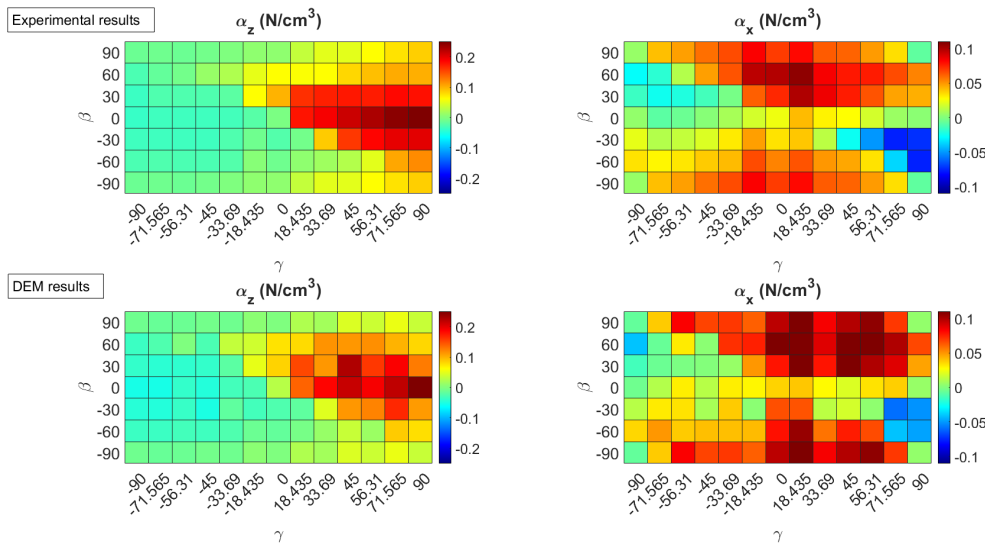


Figure 2.3: Experimental and DEM results for vertical and horizontal stresses indicate good quantitative agreement for all γ and β .

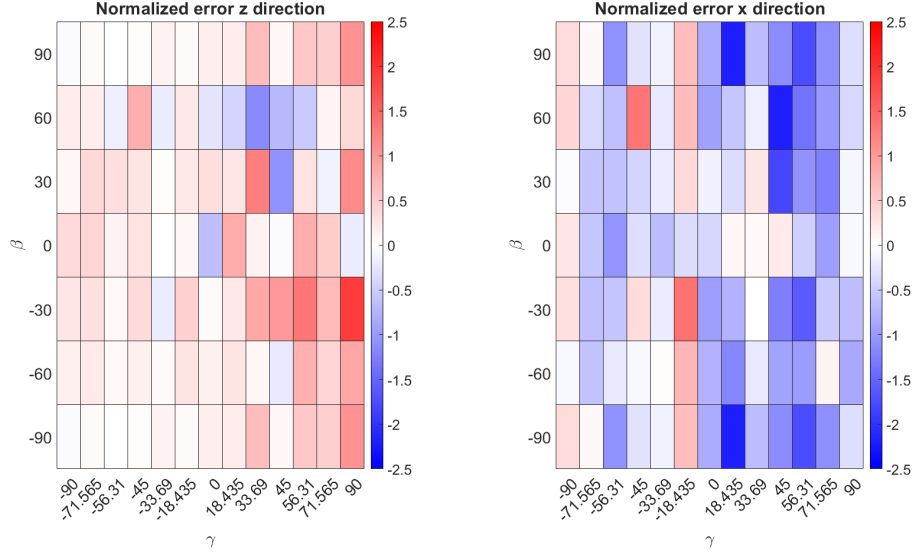


Figure 2.4: Normalized error map (see equation 2.2).

Impact velocity	α_x [N/cm ³]	α_z [N/cm ³]
Chrono (DEM) results		
1 cm/s	0.004631	0.3022
3 cm/s	0.004155	0.2851
5 cm/s	-0.01086	0.3232
Experimental results		
1 cm/s	0.0025033	0.2931

Table 2.2: Vertically-constrained ($\beta = 0, \gamma = \pi/2$) penetration results for three different velocities. Variation of α_x and α_z in three repeated trials is less than 0.003 N/cm³ in all cases.

those simulations, the simulation parameters are the same as I discussed above and the rigid plate moves downward in the vertical direction with a constant speed. The orientation of the plate was also fixed ($\beta=0$). Figure 2.2 plots σ_x and σ_z versus penetration depth z for three constant intrusion velocities V . Lines are fitted over a depth range of $2 \text{ cm} \leq z \leq 7.5 \text{ cm}$. Table 3.1 illustrates the actual mean values of three repeated trials of α_x and α_z for three velocities and the experimental results in Li's paper [3] are added to the last row for comparison. As the table shows, 1 cm/s is within three percent of Li's results [3] for α_z , but increasing the speed from 1 cm/s to 5 cm/s only changes α_z by seven percent. So, considering the time cost and the accuracy of my simulation, I choose 3 cm/s as the penetration speed for the DEM simulations.

CHAPTER 3

GROUND REACTION FORCE MODEL

Modelling the response of yielding terrains to foot contact is challenging. The resistive forces from the ground are dependent on the granular compaction [11] [12], the intruder kinematics (penetration depth and speed) [3] [13] and the intruder morphology. Reference [13] proposes that the resistive forces consist of a hydrodynamic-like term and a hydrostatic-like term, and investigates rapid intrusion by objects that change shape (self-deform) through passive and active means. [3] presents a granular resistive force theory to predict the forces on objects intruding relatively slowly (where inertial effects are negligible) with different directions and orientations.

As discussed in the second paragraph of Chapter 2, [3] proposes that the granular resistive stresses are linear with depth. To obtain their stress results, Li et al. [3] intruded a rigid thin plate into a granular bed with different plate orientations and movement directions. And then, they got stress gradients $\alpha_{z,x}(\beta, \gamma)$ (see Eq.2.1) by linearly fitting stress results at three different depth (2.54 cm, 5.08 cm, and 7.62 cm). Finally, they performed a discrete Fourier transform on $\alpha_{z,x}(\beta, \gamma)$ results over $-\pi/2 < \beta < \pi/2$ and $-\pi < \gamma < \pi$ to obtain a fitting function. In this chapter, I do something similar but use more modes to get a more accurate representation. The fitting results in this Chapter will be used for further locomoting hopper simulations of our group.

3.1 Simulation setup

The simulation setup in this chapter is identical to in Figure 2.1, which shows the planar view of the plate penetrating into the granular domain. The rigid plate is 5 cm \times 5 cm \times 0.5 cm (area = 25 cm²) and the plate mass is 0.25 kg. More details about the simulation parameters can be found in Table 3.1 and the JSON file in my GitHub repository ¹.

¹https://github.com/HappyLamb123/Foot-ROBOT/blob/master/demo_code/generate_formula/intrude/demo_GRAN_plate.json

Time step	5e-5s
Plate dimension	5 cm × 5 cm × 0.5 cm
Plate density	20 g/cm ³
Sphere radius	3 mm
Sphere density	2.6 g/cm ³
Domain size	40 cm × 30 cm × 30 cm
Sphere-sphere normal contact stiffness	1e8 N/m
Sphere-wall normal contact stiffness	1e8 N/m
Sphere-sphere normal damping coefficient	500 N s/m
Sphere-wall normal damping coefficient	500 N s/m
Sphere-sphere tangent contact stiffness	1e8 N/m
Sphere-wall tangent contact stiffness	1e8 N/m
Sphere-sphere tangent damping coefficient	500
Sphere-wall tangent damping coefficient	500
Sphere-sphere static friction coefficient	0.385
Sphere-wall static friction coefficient	0.385

Table 3.1: Parameters for Chrono granular simulations in Chapter 3.

In Chapter 2, the granular particle container is filled by particles layer by layer from bottom to top, and no further action is taken for the bed preparation. A slightly different filling procedure is used in this chapter. To prepare the bed before the plate starts moving, particles are first created and put into a container as in Chapter 2. The box shaped container's cross section is 40 cm × 30 cm and it is filled by particles to a depth of approximately 30 cm. Once particles are created and placed, they are given random initial velocities in three directions (x , y and z). The absolute velocity values for each direction are from 40 cm/s to 45 cm/s and the sign of the velocity is randomly chosen. I wait 2.5 s in order to make sure the granular bed is fully settled before starting the intrusion of the foot. Figure 3.1 shows the mean speed values of 95700 particles and their standard deviation from 0 to 9.9 s. The logarithmic mean and standard deviation can be found in Figure 3.2. As the plots show, particle velocities quickly decay to near 0, so 2.5 s is more than enough time to ensure the granular bed is fully settled.

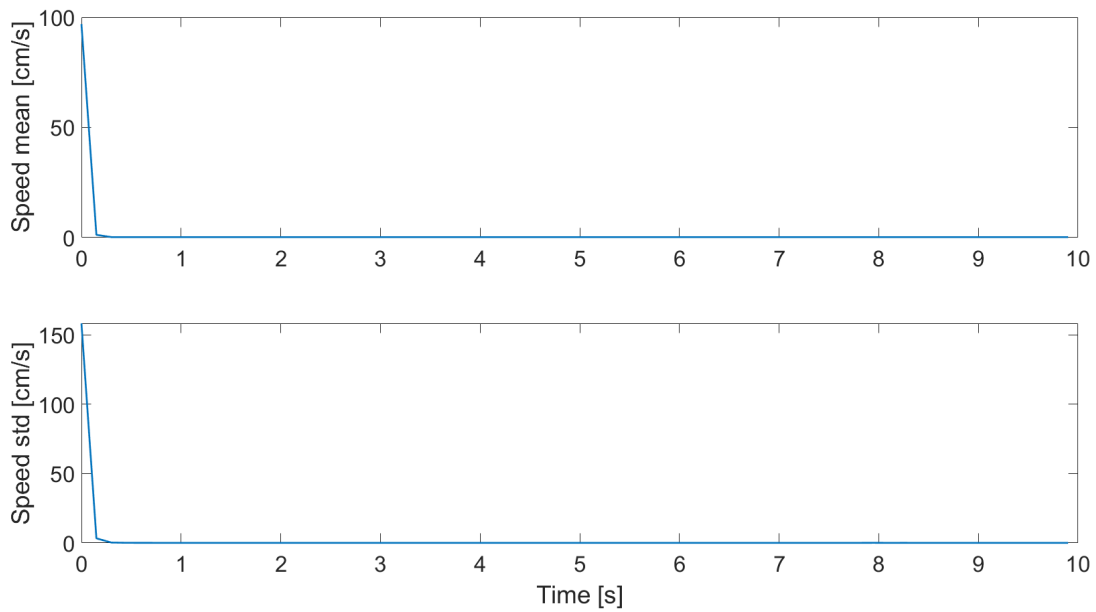


Figure 3.1: Average particle speed vs. time (upper) and particle speed standard deviation vs. time (bottom).

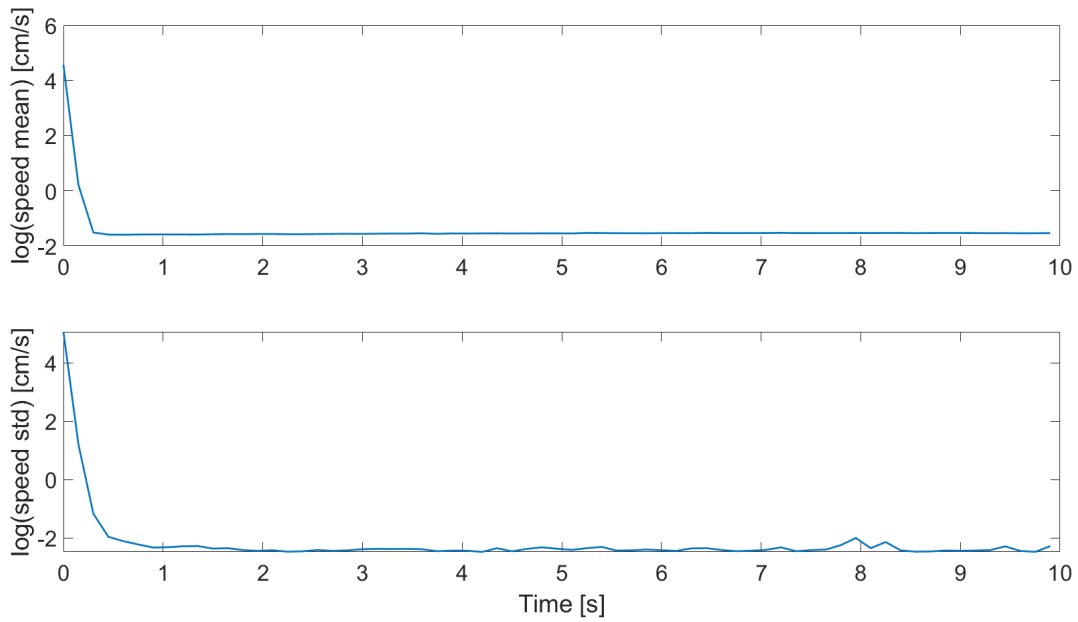


Figure 3.2: Logarithmic average particle speed vs. time (upper) and logarithmic particle speed standard deviation vs. time (bottom).

3.2 Resistive forces fitting functions

To get analytic expressions for $\alpha_{x,z}$ in Eq.2.1, I did hundreds of DEM simulations with different attack angles β and intrusion angles γ which vary from -90 degrees to 90 degrees. The constant intrusion speed is chosen as 3 cm/s. For each $\beta - \gamma$ pair, I did three repeat trials, and took the average of $\alpha_{x,z}$, as in Chapter 2, and then I took absolute values of those $\alpha_{x,z}(\beta, \gamma)$ data. Figure 3.3 plots $|\alpha_{x,z}(\beta, \gamma)|$. In Figure 3.3, the upper two plots show the α_z and α_x change with different β and γ . I took absolute values of the raw data because the stress results change rapidly when the plate switches from intruding to extracting because the stresses changes from positive to negative. For a small number of modes, the Fourier transform is unable to capture this rapid change. However, since the resistive forces are always opposite to the plate's moving direction, I can easily find the correct resistive forces direction given the plate's velocities. Thus, it's reasonable to take absolute values of the raw data to reduce Fourier fitting errors. By performing discrete Fourier transform on the processed raw $\alpha_{z,x}$ data over $-\pi/2 < \beta < \pi/2$ and $-\pi < \gamma < \pi$, I can obtain a fitting function. To balance the accuracy and conciseness of the fitting formulas, I set the Fourier transform order as 2. The fitting functions are:

$$\alpha_z(\beta, \gamma) = \sum_{m=-2}^2 \sum_{n=-2}^2 [A_{m,n} \cos(2m\beta + n\gamma) + B_{m,n} \sin(2m\beta + n\gamma)], \quad (3.1)$$

$$\alpha_x(\beta, \gamma) = \sum_{m=-2}^2 \sum_{n=-2}^2 [C_{m,n} \cos(2m\beta + n\gamma) + D_{m,n} \sin(2m\beta + n\gamma)], \quad (3.2)$$

where $A_{m,n}$, $B_{m,n}$, $C_{m,n}$ and $D_{m,n}$ are coefficients of the fitting function and can be found in Table 3.2. The coefficients for 1st order and 3rd order Fourier fitting can be found in this Google drive file ².

To determine the accuracy of the fitting formulas, I generated error maps as shown in Figure 3.4 to Figure 3.6. Errors for each $\beta - \gamma$ pair in the error maps are computed as: α_z (α_x) - Fourier

²https://drive.google.com/file/d/1T4itiIVEqeF11zM6uPIz8_AqbE3kJiTj/view?usp=sharing

m	n	$A_{m,n}$	$B_{m,n}$	$C_{m,n}$	$D_{m,n}$
0	0	0.0587405	0	0.0510357	0
0	1	-0.000449	0.0256221	0.0002929	0.0062092
0	2	-0.007932	-0.000897	0.0021059	-0.0005
0	-2	-0.007932	0.0008966	0.0021059	0.0004998
0	-1	-0.000449	-0.025622	0.0002929	-0.006209
-1	0	0.0308869	-0.0081	-0.009617	-0.007194
-1	1	0.0023856	0.0152946	0.0026648	0.0054052
-1	2	-0.003031	-0.005611	-0.002222	-0.003655
-1	-2	-0.00331	-0.004783	-0.002184	-0.003597
-1	-1	-0.002843	-0.016151	-0.002984	-0.005976
-2	0	0.0050729	-0.00493	-0.007099	-0.002165
-2	1	0.0013374	0.0052393	0.0015156	-0.005303
-2	2	-1.17E-05	-0.003304	0.0020161	-0.000657
-2	-2	-0.000354	-0.003454	0.0017459	-0.001073
-2	-1	-0.001479	-0.005812	-0.001452	0.0051538
2	0	0.0050729	0.0049298	-0.007099	0.0021647
2	1	-0.001479	0.0058119	-0.001452	-0.005154
2	2	-0.000354	0.0034541	0.0017459	0.0010725
2	-2	-1.17E-05	0.0033043	0.0020161	0.0006572
2	-1	0.0013374	-0.005239	0.0015156	0.0053032
1	0	0.0308869	0.0080999	-0.009617	0.0071942
1	1	-0.002843	0.0161505	-0.002984	0.0059762
1	2	-0.00331	0.0047832	-0.002184	0.0035974
1	-2	-0.003031	0.0056105	-0.002222	0.0036552
1	-1	0.0023856	-0.015295	0.0026648	-0.005405

Table 3.2: Coefficients for 2nd order Fourier filtered force functions.

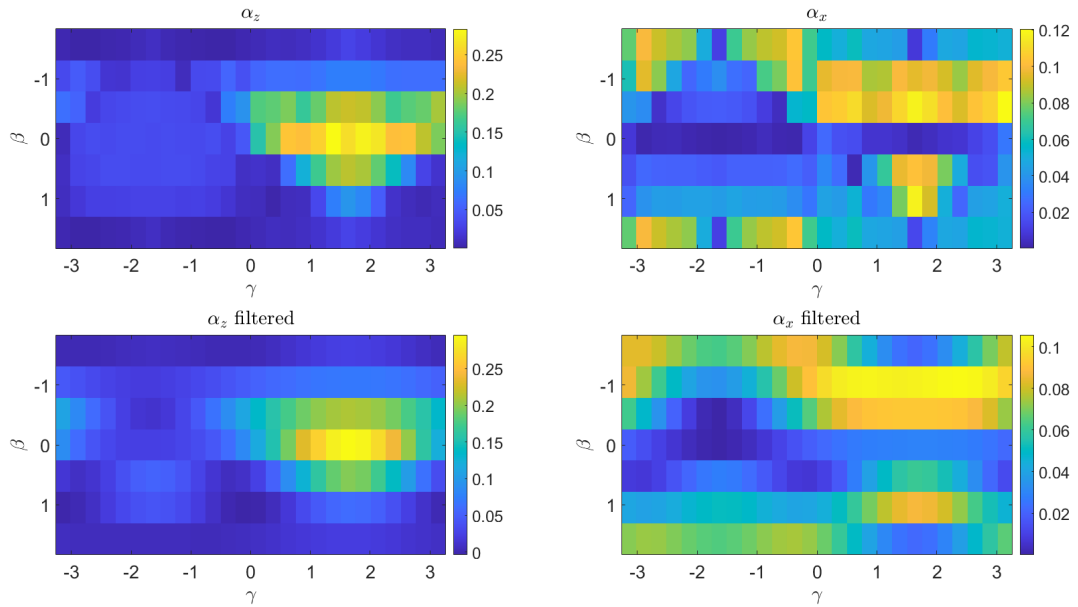


Figure 3.3: Raw (top row) and Fourier filtered (bottom row) $\alpha_{z,x}$ colormaps (γ and β values are in radians). Colorbar units are in N/cm^3 .

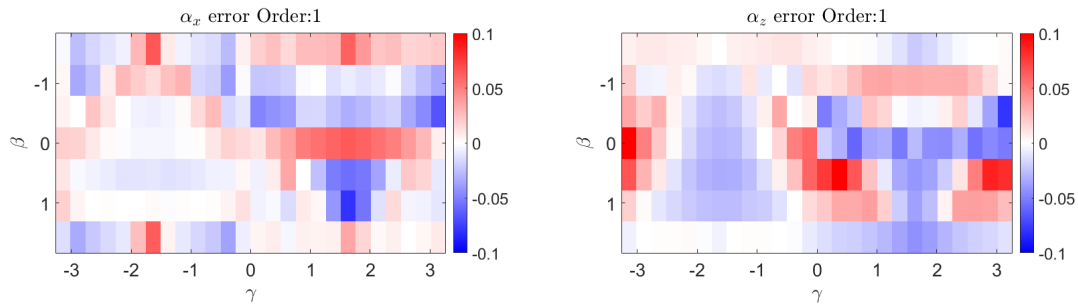


Figure 3.4: 1st order $\alpha_{z,x}$ error maps (γ and β values are in radians). Colorbar units are in N/cm^3 .

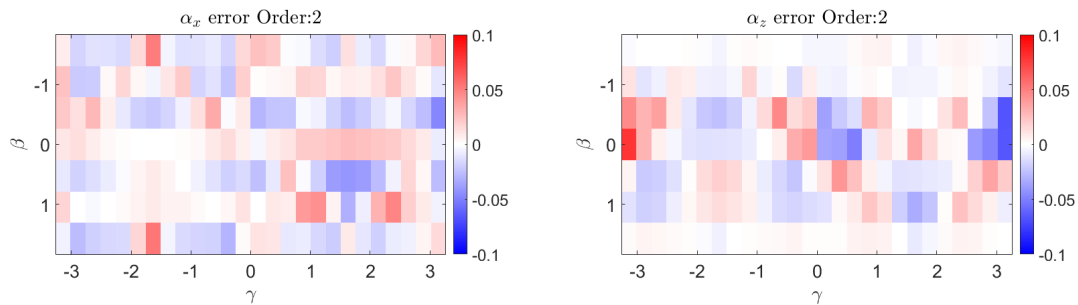


Figure 3.5: 2nd order $\alpha_{z,x}$ error maps (γ and β values are in radians). Colorbar units are in N/cm^3 .

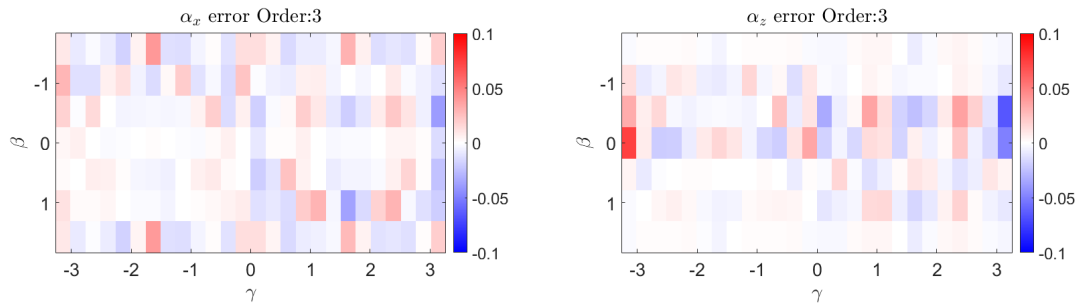


Figure 3.6: 3rd order $\alpha_{z,x}$ error maps (γ and β values are in radians). Colorbar units are in N/cm^3 .

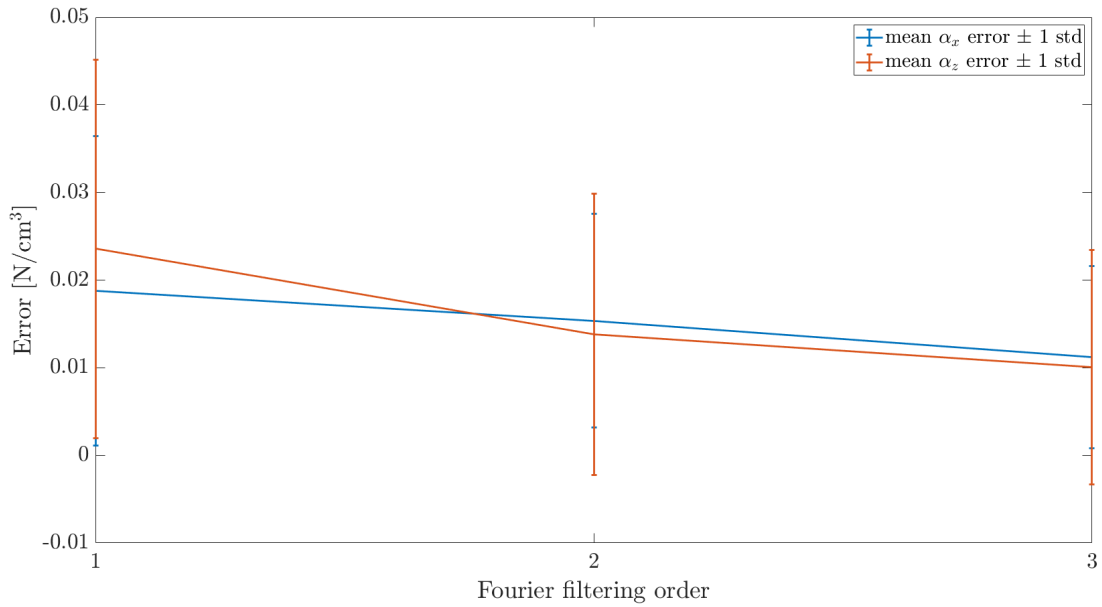


Figure 3.7: Mean error between $\alpha_{x,z}$ from raw data and from Fourier representation vs. number of modes.

fitted α_z (Fourier fitted α_x). By comparing the error maps of three Fourier fitting orders, one can see that a second order fit ensures the fitting formula accuracy while limiting the number of fitting parameters. As Figure 3.5 shows, errors in most regions are close to zero (less than 0.02) and only errors of α_z near $\gamma = \pm\pi$ are near 0.1 N/cm³. At the boundaries of the $\beta - \gamma$ plane, the physical meaning is the plate switches between extraction and intrusion. It is more difficult to intrude than withdraw, so the values near boundaries see a rapid change along γ . However, low order Fourier fits are less accurate if the raw data changes rapidly. This is why the fit is less accurate near boundaries. Figure 3.7 shows that the mean and standard deviation of the absolute errors for order 2 is less than 0.0211 N/cm³, so the 2nd-order Fourier series approximation can be used as a fast-to-evaluate model of granular resistive stresses, at least for low intrusion velocities and away from the effects of boundaries.

CHAPTER 4

PERIODIC HOPPING OF A MONOPOD

Many applications for mobile robots involve environments that are dangerous or unsuitable for humans. Moreover, due to the inaccessible/unsafe nature of these environments, level rigid ground is rare, so wheeled/treaded robots are often unsuitable due to limited mobility. Legged robots would seem the ideal choice, except that the bulk of research and development of legged robots has focused on hard-ground applications, which are of little use in these challenging environments. In many cases, the terrain is not rigid but, rather, is some kind of deformable granular substrate (e.g., sand, soil, or snow). While there has been recent progress on legged robotic locomotion on these kinds of substrates (e.g., [3], [13], [5], [6]), a major remaining challenge with hopping/walking/running on these substrates is that they do not return to their pre-impact state. This represents a permanent energy loss as well as a challenge to maintaining stable gaits. In addition to its relevance to legged locomotion on deformable terrain, this unidirectional ground response represents an interesting variation on the classic “bouncing ball problem” in hybrid dynamics [14],[4]. While there are many tools for generating and analyzing cyclic trajectories in hybrid dynamical systems (e.g., Poincare analysis, Lyapunov analysis), I bring the tools of trajectory optimization [5] and discrete-element-method (DEM) simulation to bear on the problem. Specifically, I formulate the search for vertically-constrained hopping gaits on deformable terrain as a trajectory optimization problem with boundary constraints. I solve this problem numerically, obtaining a feedforward control signal. Then, in DEM simulation, I apply this feedforward control signal along with a stabilizing time-invariant feedback law.

In this chapter, I develop a control strategy for a vertically-constrained monopod robot hopping on non-cohesive frictional granular media. The robot is released from the apex of its trajectory and then impacts the bed with velocities ranging from 0 to -4 m/s. When the foot contacts the granular bed, the ground reaction forces are modeled by RFT. Then the equations of motion of the robot has

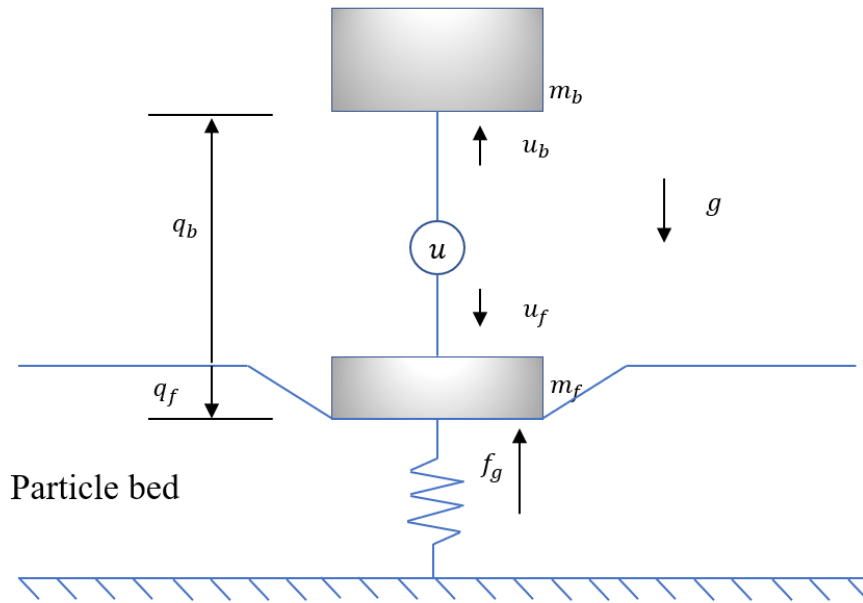


Figure 4.1: Physical models of the monopod robot and soft ground. The soft ground is treated as a unidirectional spring with stiffness k_g , see Eq. 4.1. The body, located at height q_b above the undisturbed ground, has mass m_b , and the foot, located at height $-q_f$ below the undisturbed ground, has mass m_f . Body and foot are connected with a linear motor which exerts a possibly time dependent and equal and opposite force u on both masses. Heights q_b and $-q_f$ are measured relative to the undisturbed ground surface.

a closed-form solution. The trajectory optimization treats the equations of motion as a part of the equality constraints and produces feedforward control efforts for the robot. Finally, the center of mass (CoM) of the robot can be controlled to return to the initial apex with zero speed after both a single hop and five hops. Both single hop and five hops are tested in DEM using both feedforward and feedforward + feedback control strategies.

4.1 Soft ground model

Eq. 2.1 shows that the horizontal and vertical resistive forces increase linearly with the intrusion depth. For a 1D hopping monopod robot, the granular substrate can be modeled as a unidirectional

Foot dimension	5 cm x 5 cm x 10 cm
Foot mass	0.25 kg
Body dimension	5 cm x 5 cm x 5 cm
Body mass	1.25 kg
Stroke limit	0.5 m

Table 4.1: Physical properties of the monopod robot.

spring. The ground resistive force f_g is expressed as

$$f_g = \begin{cases} 0 & \text{flight} \\ -k_g q_f & \text{yielding} \\ [0, -k_g q_f] & \text{static} \end{cases} \quad (4.1)$$

where k_g is the ground stiffness. The area of the foot is 25 cm^2 and the stress gradient $\alpha_z(\beta = 0, \gamma = 90^\circ)$ is 0.25 N/cm^3 . I chose $k_g = 25 \text{ cm}^2 \times 0.25 \text{ N/cm}^3 \times 100 = 625 \text{ N/m}$ to match the experimental data in Chapter 3 I ignore the withdraw force when lift off the robot. The foot thickness is chosen to ensure no particles can accumulate on the top of the foot, which helps to reduce the withdraw stresses.

4.2 Robot model

To focus on foot-ground interaction rather than whole-body control, I study a simple monopedal robot hopping vertically as illustrated in Figure 4.1. The robot consists of a body (position q_b and mass m_b) and a flat-bottomed foot (position q_f and mass m_f) connected by a linear motor (idealized as a source of force u) such that $u > 0$ pushes the two masses apart. The dimensions and masses of the robot foot and body can be found in Table 4.1. The stroke limits of the robot system are

$$0 < q_b - q_f < 0.5 \text{ m}. \quad (4.2)$$

The hybrid dynamics of the hopping robot are divided into three phases: flight, yielding stance, and static stance. Figure 4.2, reproduced from [8], describes the conditions for transitioning between

flight, yielding stance, and static stance. Phase transitions depend on the foot kinematics and the control effort. My robotic task is represented by periodicity constraints on the CoM position and velocity, but during flight, I have no control over the CoM trajectory. Thus, any attempt to influence the flight-phase CoM trajectory must happen during stance. Therefore, I restrict my analysis to the static and yielding stance phases. The equations of motion for the two stance phases are,

$$\ddot{q}_b = \frac{u}{m_b} - g, \text{ and} \quad (4.3)$$

$$\ddot{q}_f = \frac{f_g}{m_f} - \frac{u}{m_f} - g, \quad (4.4)$$

where g is the gravitational acceleration (9.81 m/s^2). For the following section on robot control, initial conditions are,

$$q_b(0) = 0.25 \text{ m}, q_f(0) = 0 \text{ and } \dot{q}_b = \dot{q}_f = V_0, \quad (4.5)$$

where V_0 is the impact velocity.

4.3 Robot control

My first task is to find period one hopping gaits for the vertically-constrained monopod robot. Gait generation is the formulation and selection of a sequence of coordinated leg and body motions that propel a legged robot along a desired path [15]. Specifically, my robot starts impact at a certain initial position and moves vertically downward with an initial impact velocity. The desired motor control periodically returns the robot to the initial impact position with the same CoM velocity magnitude but in the upward direction on each successive hop.

There are various methods of determining the control signal $u(t)$ that results in periodic hopping trajectories (e.g., Poincare analysis [16], Lyapunov analysis), but I use trajectory optimization [17] to find controls and trajectories that satisfy periodicity constraints.

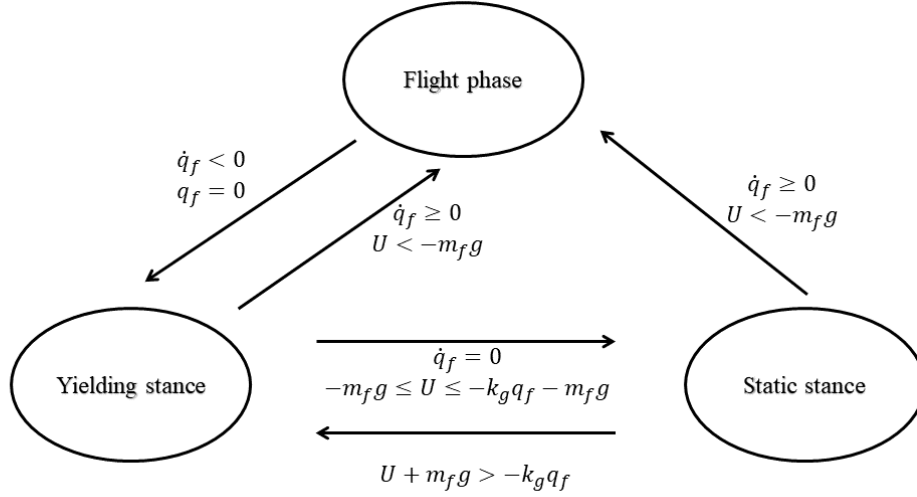


Figure 4.2: Transitions between flight phase, yielding stance and static stance. Reproduced from [8] with permission.

4.3.1 Feedforwr control

To determine the open loop control signal for the robot, I divide the problem into two parts, stance phase and flight phase. The stance-phase optimal control problem can be transformed into a constrained nonlinear program. For the flight phase, no ground forces are applied to the foot, the velocity of body and foot is expected to be equal, and the distance between the body and foot should return to the initial value, so analytic methods are used to determine the corresponding control signal.

Hubicki et al. [5] describe a fast optimal motion planning algorithm for a 1D hopping robot. By formulating an optimal control problem as a constrained nonlinear program (NLP), I utilize a well-developed NLP solver (i.e., MATLAB fmincon) to find out the control signal. Control signals $u(t)$ are chosen as fourth order polynomials because the system has 4 constraints, which determine 4 coefficients of the polynomials. The remaining coefficient is determined by optimizing the cost

function. The expression is as follows,

$$u(t) = a + bt + ct^2 + dt^3 + et^4, \quad (4.6)$$

where $\mathbf{x} = [a, b, c, d, e]$ are the design variables of the NLP. Note that I fix the time at 0.3 s for the stance phase and optimize the coefficients of the control signals $u(t)$ to satisfy the constraints. I choose 0.3 s because it can ensure my MATLAB code to find a solution for the optimal control. For a longer time like 1s can also make the optimization problem converge but it needs more time to solve. In addition, too short a stance time will not be able to develop enough momentum for the robot to jump back to apex given stroke constraints and lack of rate dependence in GRF model.

I choose control effort squared as the cost function:

$$J(\mathbf{x}) = \int_0^{T_s} u^2(t) dt, \quad (4.7)$$

Reference [8] chooses intrusion depth of the foot as the cost function. I choose the control effort squared because it makes the cost function convex which is good for the convergence of the optimization problem. The resulting formation for the stance-phase nonlinear program is as follows:

$$\begin{aligned} \mathbf{x}^* &= \arg \min_{\mathbf{x}} J(\mathbf{x}) \quad \text{s.t.} \\ f(\mathbf{x}) &= 0, \\ g(\mathbf{x}) &\leq 0, \end{aligned} \quad (4.8)$$

where $f(\mathbf{x})$ are the equality constraints obtained by the robot dynamics (see Eq. 4.3 and Eq. 4.4) and robot boundary conditions, $g(\mathbf{x})$ are the inequality constraints obtained by the linear controller control limits and robot stroke limits (see 4.2), and T_s is the desired stance-phase period.

The stance-phase terminal conditions at T_s are

$$q_b(T_s) = C, q_f(T_s) = D, \dot{q}_b(T_s) = E \text{ and } \dot{q}_f(T_s) = 0, \quad (4.9)$$

$q_f(0)$	0 m	$\dot{q}_f(0)$	-0.2 m/s
$q_b(0)$	0.25 m	$\dot{q}_b(0)$	-0.2 m/s
$q_f(T)$	0 m	$\dot{q}_f(T)$	0.2 m/s
$q_b(T)$	0.25 m	$\dot{q}_b(T)$	0.2 m/s

Table 4.2: Boundary conditions

where $[C, D, E]$ (terminal body position, terminal foot position, and terminal body velocity respectively) are constants determined by ground stiffness and impact velocity. One thing interesting is my robot never leaves ground in the stance phase because I add constraints in the MATLAB solver to do this.

The flight phase control first applies a constant forces to the foot and body, and then turns off the linear motor during the remainder of free fall. I choose this strategy for the flight phase because the solution for control efforts is easily obtained. Once given the depth of the foot at the end of the stance phase and the lift-off acceleration of the foot, I can solve for the control efforts for lift-off and the terminal states of the body in the stance phase.

By setting the stance-phase duration to 0.3 s and boundary conditions as given in Table 4.2, I obtain the control efforts and the resulting body and foot trajectories shown in Figure 4.3. As those results are for an example impact velocity of -0.2 m/s, the foot and the body move downwards from the top of the granular media. The control signals make the foot and the body return to the initial height while the terminal speed values are the same as the initial speed. We can also observe the double intrusion of the foot, which is an interesting feature of locomoting on soft ground.

4.3.2 Feedforward plus feedback control

After testing the open loop control forces in Chrono simulation, I found that the trajectories of the robot deviate from the expected ones because the ground stiffness approximation is not sufficiently accurate. Therefore, I introduce a feedback controller to stabilize control in stance phase. So, the control strategy is feedforward plus feedback control now.

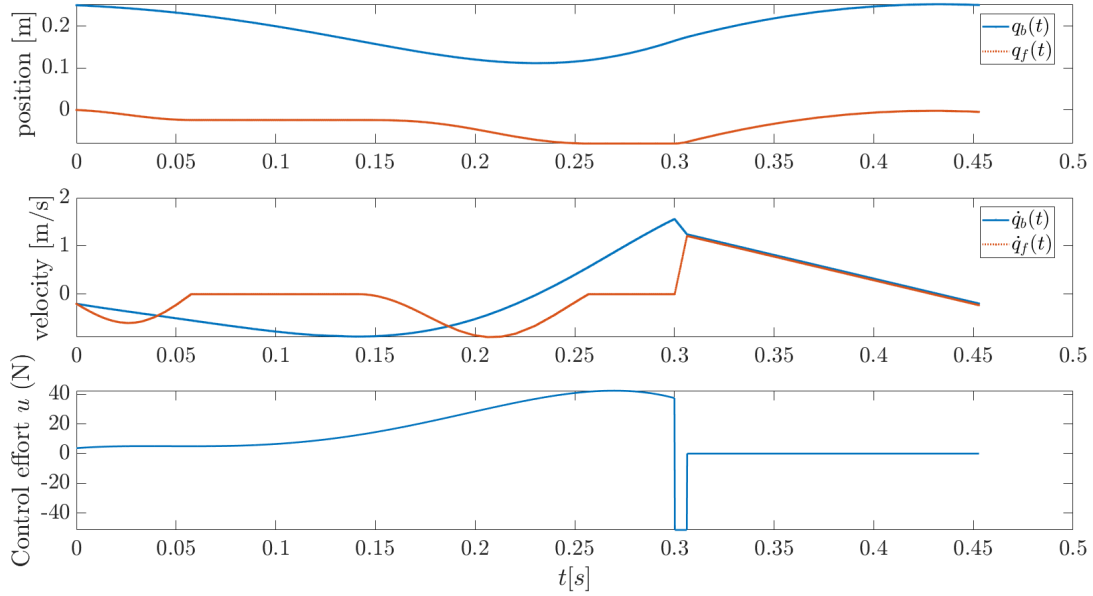


Figure 4.3: Planned foot and body states vs. time (upper and middle plots) and planned control efforts vs. time (bottom plot).

As Figure 4.4 shows, the control system inputs are the desired center of mass(CoM) position and velocity of the robot. The desired CoM states($q_{CoM,d}$ and $\dot{q}_{CoM,d}$) are generated from MATLAB when I apply the open loop control forces to the robot in numerical simulation. The difference between the desired robot states and the actual robot states (q_{CoM} and \dot{q}_{CoM}) are the CoM errors($q_{CoM,e}$ and $\dot{q}_{CoM,e}$). By passing those errors into a PD controller, I obtain the feedback control forces U_{FB} as illustrated in Fig.4.4. In the section above, I use trajectory optimization to get the feedforward control forces(U_{FF}). Combining the feedback and feedforward control forces and adding the new forces(U) into the equations of motion of the robot system, I get the real-time states of the robot.

I implement this feedforward plus feedback controller on my robot model in Chrono. Specifically, I create a robot model like Figure 4.1 with physical properties as given in Table 4.1. I set the impact velocity of both the body and the foot to -0.2 m/s. When the robot transitions from stance phase to flight phase, the CoM position is expected to return to 0, and the CoM velocity is expected to be 0.2 m/s. Since no external force is applied to the robot system during the flight phase, the robot can

return to the initial position with the same velocity because of momentum conservation. The two conditions thus ensure the robot hops periodically. For the open loop control case, I applied the feedforward control forces generated from MATLAB. For the feedforward plus feedback case, I add a PD controller on the robot to track the CoM of the robot. As Figure 4.5 shows, my controller significantly reduce both the CoM position and velocity errors.

To quantitatively analyze the error of the two control strategies (i.e. feedforward and feedforward+feedback), I test their performance for different impact velocities(from -4 m/s to -0). The errors are computed as the terminal CoM position/velocity of the two control methods in Chrono minus the desired terminal CoM position/velocity from MATLAB. For the feedforward plus feedback control, I run Chrono simulation for 3 trials to analyze its uncertainty. As Figure 4.6 shows, my strategy works well in reducing the error for different impact velocities compared to the open loop control alone.

In addition, I investigate how different foot sizes influence the performance of my controllers. As the foot size decreases toward the particle size, force fluctuations increase and present greater challenges to the controllers. To investigate the efficacy of the controller, I test three foot sizes (1 cm x 1 cm, etc.) in addition to the original 5 cm x 5 cm foot. To ensure the foot reach the same depth for different foot sizes, I scale the mass of the foot and the body based on the nondimensionalization method in [8]. The ratio of the total mass of the robot to the foot square area is fixed. For each foot size, I test six different impact velocities(0, -0.2m/s, -0.5m/s, -1m/s, -2m/s and -4m/s) and conduct three trials for each impact velocity. Both the feedforward + feedback controller and the open loop controller are tested in these experiments. The CoM position error percentage is computed as Eqs. 4.10,

$$\eta = \frac{q_{CoM,i}(T) - q_{CoM,d}(T)}{q_{CoM,d}(T)} \times 100\%, \quad (4.10)$$

where i can be feedforward + feedback or feedforward alone, d is the desired CoM position generated from MATLAB, and T is the duration of one hop. For each foot size, I compute the mean values and standard deviations of all the error percentages of all impact velocities, and draw error-bars as shown in Figure 4.7. Again, I observe that the feedforward plus feedback controller reduces

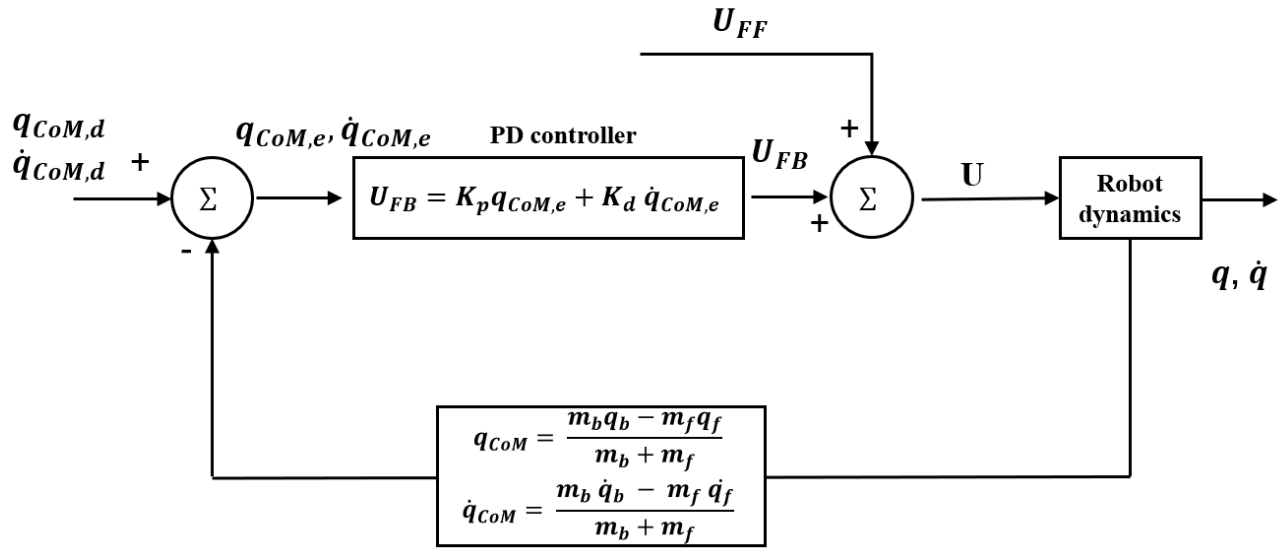


Figure 4.4: Block diagram of feedforward plus feedback control for stance phase. q_{CoM} and \dot{q}_{CoM} are the center of mass position and velocity, respectively. q_{CoM} , $q_{CoM,d}$, and $q_{CoM,e}$ are actual center of mass position, desired position and position error, respectively. U_{FB} and U_{FF} are the feedback and feedforward control forces, respectively.

the error to less than 2% in all cases. This indicates my controller is robust for different foot sizes, even in the presence of large variations in the ground reaction force when the foot is small.

4.4 Multiple hops

The ultimate goal of my work is to design gaits for monopod hopping on deformable ground. For the single hop in the sections above, the robot jumps on undisturbed ground. To challenge my feedforward + feedback controller, I make the monopod to have five hops on disturbed ground. As Section 4.3.2 shows, I successfully implemented my feedforward plus feedback controller on the robot for single hop. Figure 4.3 shows expected trajectories of a single hop of the monopod. The robot starts hopping with impact velocities of -0.2 m/s and returns to the initial position with the same velocity. My control strategy for multiple hops is to track the CoM trajectories of the single hop of the robot in each hop. In each hop of a multi-hop sequence, I set the period equal to the duration of expected trajectories from MATLAB and use my feedforward plus feedback controller to stabilize my control in stance phase. For the flight phase, I add a PD controller to make the

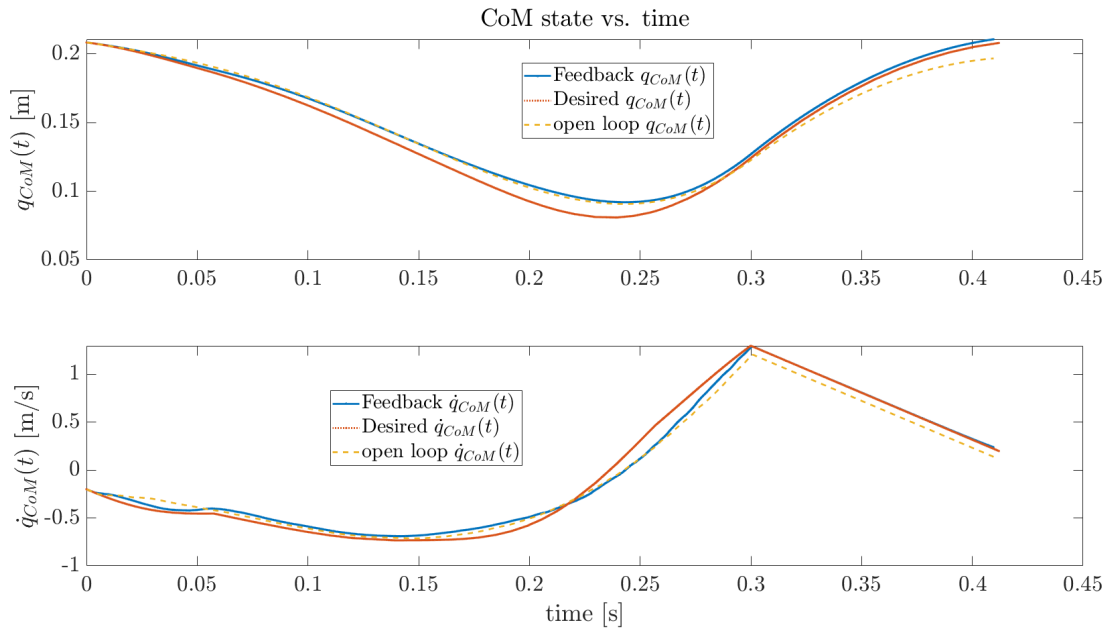


Figure 4.5: CoM trajectories from optimal(desired) and for two control strategies. Upper plot: CoM position vs. time. Bottom plot: CoM velocity vs. time. Blue, red and yellow curves are feedforward plus feedback results, expected results from MATLAB and feedforward control results, respectively.

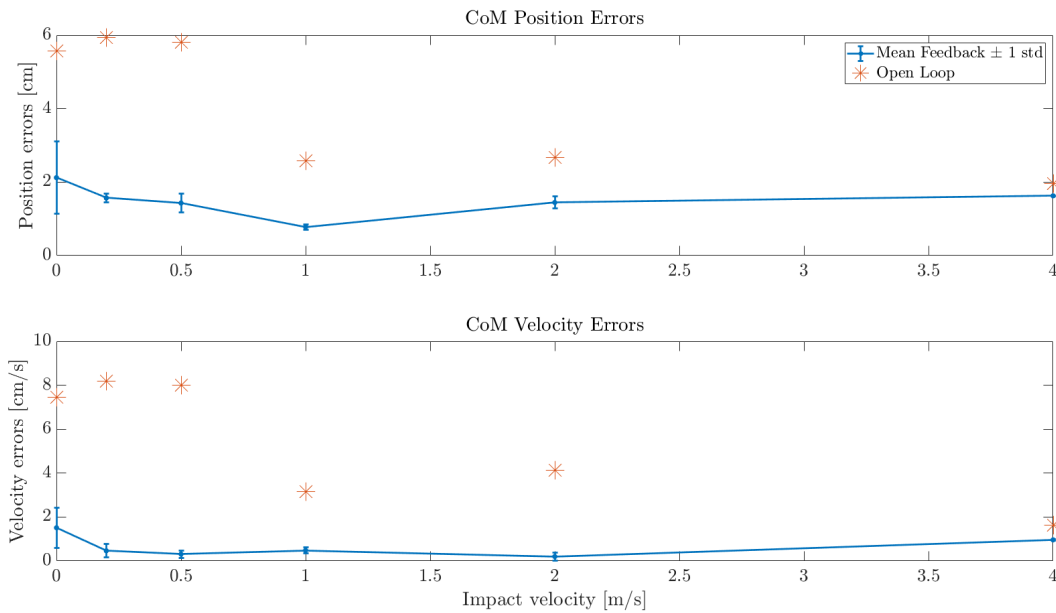


Figure 4.6: Position and velocity errors of two different control strategies for multiple impact velocities. Asterisks are errors of open loop control while error bars are errors of feedforward plus feedback control.

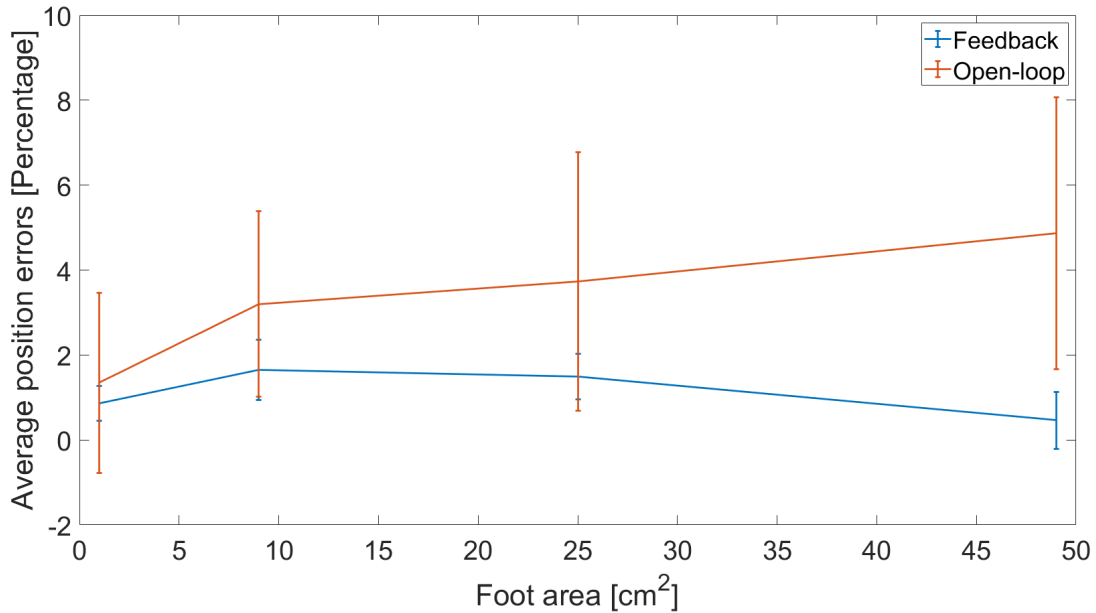


Figure 4.7: Experimental errors in CoM position from Eq.4.10 vs. foot size.

velocity of the body and foot equal, and make the body-foot distance equal to the initial value. Figure 4.8 compares the CoM trajectories of two control strategies. The robot starts moving with an impact velocity of -0.2 m/s. The feedforward plus feedback controller has far greater performance than the open loop controller. After five hops, the CoM trajectories of the robot tracks the expected trajectories quite well.

To compare the errors associated with the two control strategies, I compute the errors as CoM position/velocity at the end of five hops minus the expected terminal CoM position/velocity. To ensure my controller is robust for different impact velocities, I test impact velocities ranging from -4 m/s to 0 . For each impact velocity, I run Chrono simulation for three trials. Figure 4.9 shows errorbars of both CoM position and CoM velocity after five hops for each impact velocity. The errors of the feedforward plus feedback controller are quite close to zero for all the impact velocities I tested. This again shows the robustness of my controller. In addition to the plots in this chapter, I also made corresponding videos of the robot hopping in Chrono. The first video¹ shows five hops on

¹https://drive.google.com/file/d/1LkUFWx_U1X0XtGNpdf6Dcj_IhaWzxXH/view?usp=sharing

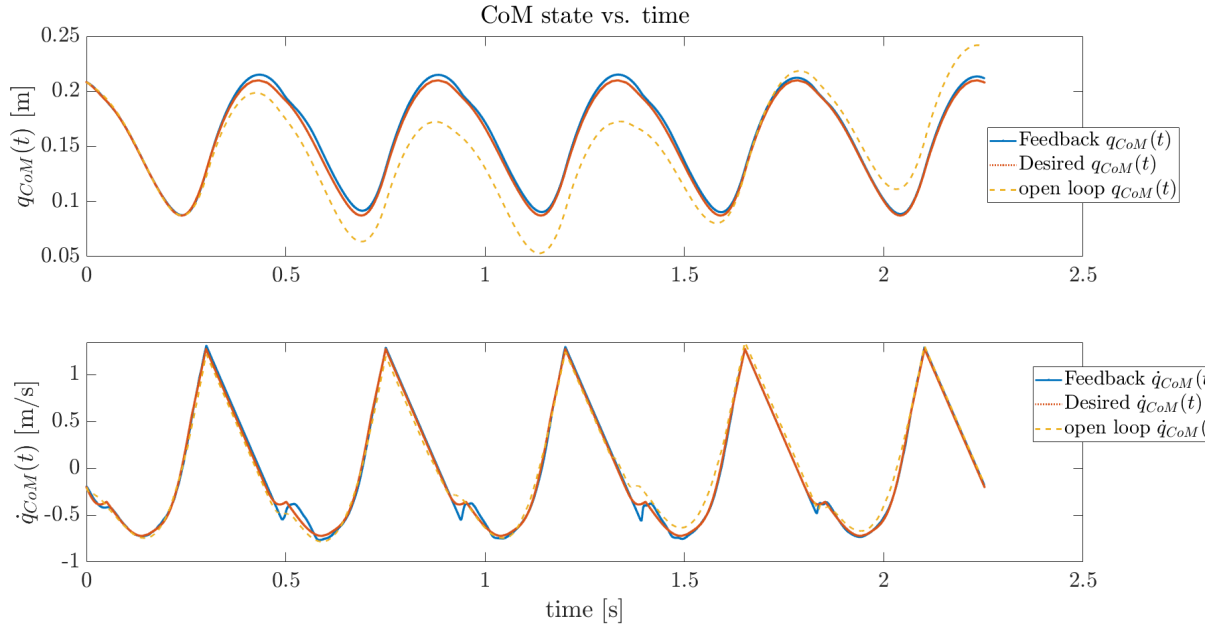


Figure 4.8: Center of mass trajectories for five hops. Upper plot: CoM position vs. time. Bottom plot: CoM velocity vs. time. Blue, red and yellow curves are feedforward plus feedback results from Chrono, expected results from MATLAB, and feedforward control results from Chrono, respectively.

soft ground using a feedforward plus feedback controller. The robot in the second video² is controlled by an open loop controller. Figure 4.10 is the screenshot of one demo video. Comparing the two videos shows that the feedback controller works well making the CoM to reach the expected height.

²https://drive.google.com/file/d/1E8iMqUuT_bcmHaP9IYCvcwEjnf4R89iO/view?usp=sharing

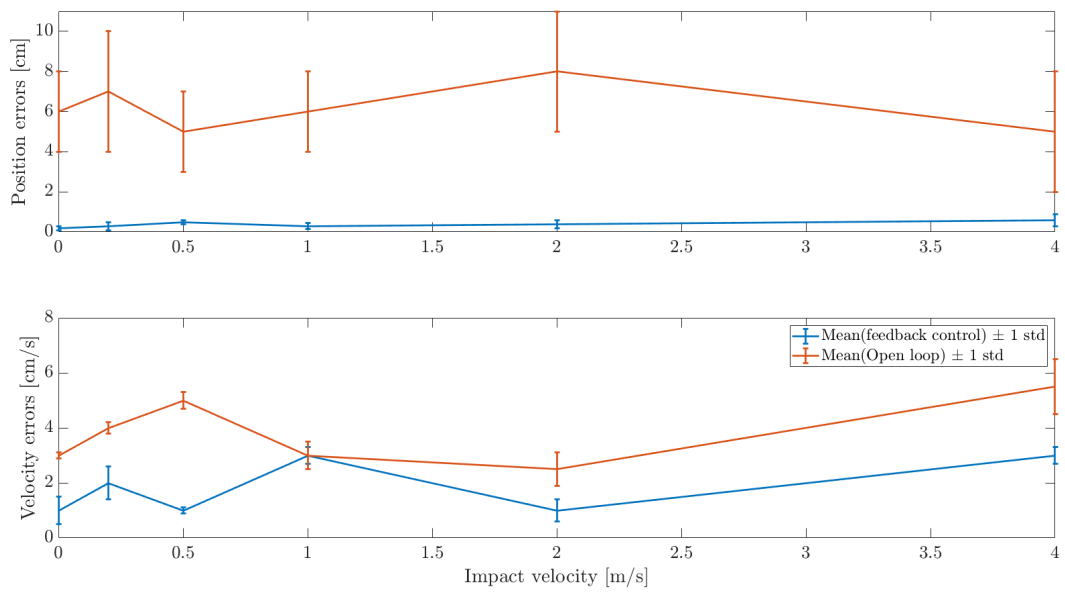


Figure 4.9: Errorbar of robot CoM trajectories after five hops for different impact velocities under open loop (orange) and feedforward plus feedback (blue) control.

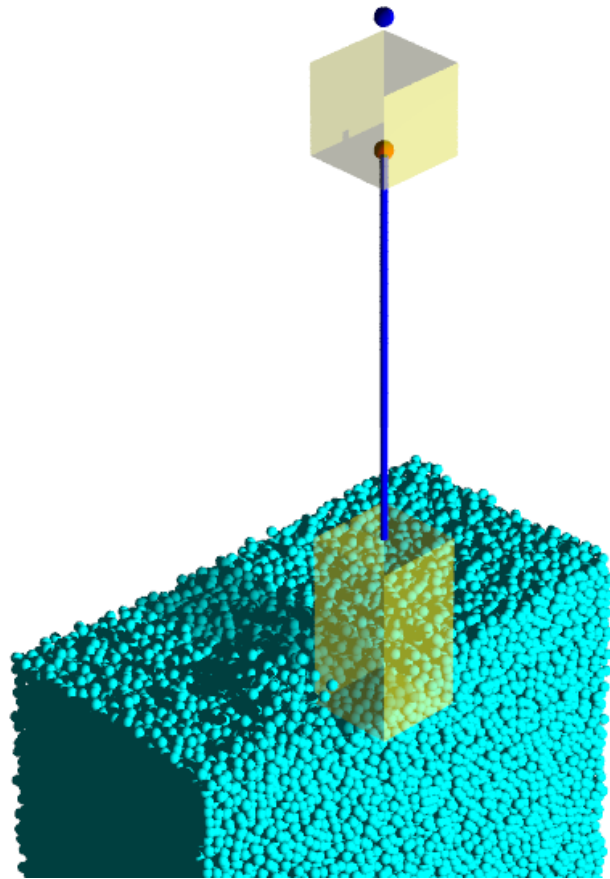


Figure 4.10: Screenshot of demo video. Upper yellow box is the body while bottom yellow box is the foot. The blue line represents the linear motor which connects the body and the foot. Red sphere is the real time position of the CoM of the robot. The blue sphere is the desired apex for the CoM.

CHAPTER 5

CONCLUSION

In this work, I set up a DEM based simulation environment called Chrono. To validate its reliability and accuracy, I ran many simulations and compared my results with results in [3]. The simulation results have a good match to experimental results. After that, I utilized Chrono to generate a ground stiffness approximation formula based the ground resistive force model in [3]. I also formulated a soft-landing problem and develop solutions to design open loop periodic gait for our monopod hopper with the trajectory optimization and the approximation formula. Then I develop a new control solution by applying feedforward plus feedback control on the monopod robot. The new control strategy is tested on single hops and multiple hops for various impact velocities in Chrono simulation. The Chrono simulation results indicate our controller is robust and can reduce CoM trajectory errors.

This work proves controlling a monopod to desired height periodically when hopping on yielding terrain is possible. However, our solution for the control force is not optimal, at least in terms of the energy lost to ground. My feature plan is to seek the optimal control that ensures the periodically hopping while minimizes the intrusion depth. Besides, all the experimental results I got are based on DEM simulation. It's interesting to carry out experiment validation on a real robot.

REFERENCES

- [1] J. W. Grizzle, J. Hurst, B. Morris, H. Park, and K. Sreenath, “Mabel, a new robotic bipedal walker and runner,” in *2009 American Control Conference*, 2009, pp. 2030–2036.
- [2] I. R. Manchester, U. Mettin, F. Iida, and R. Tedrake, “Stable dynamic walking over rough terrain,” in *Robotics Research*, C. Pradalier, R. Siegwart, and G. Hirzinger, Eds., Berlin, Heidelberg: Springer Berlin Heidelberg, 2011, pp. 123–138, ISBN: 978-3-642-19457-3.
- [3] C. Li, T. Zhang, and D. I. Goldman, “A Terradynamics of Legged Locomotion on Granular Media,” *Science*, vol. 339, no. 6126, pp. 1408–1412, 2013.
- [4] J. Aguilar, A. Lesov, K. Wiesenfeld, and D. I. Goldman, “Lift-off dynamics in a simple jumping robot,” *Phys. Rev. Lett.*, vol. 109, p. 174 301, 17 2012.
- [5] C. M. Hubicki, J. J. Aguilar, D. I. Goldman, and A. D. Ames, “Tractable terrain-aware motion planning on granular media: An impulsive jumping study,” in *2016 IEEE/RSJ International Conference on Intelligent Robots and Systems (IROS)*, 2016, pp. 3887–3892.
- [6] X. Xiong, A. D. Ames, and D. I. Goldman, “A stability region criterion for flat-footed bipedal walking on deformable granular terrain,” in *2017 IEEE/RSJ International Conference on Intelligent Robots and Systems (IROS)*, 2017, pp. 4552–4559.
- [7] S. F. Roberts and D. E. Koditschek, “Reactive velocity control reduces energetic cost of jumping with a virtual leg spring on simulated granular media,” IEEE, 2018.
- [8] D. J. Lynch, K. M. Lynch, and P. B. Umbanhowar, “The soft-landing problem: Minimizing energy loss by a legged robot impacting yielding terrain,” *IEEE Robotics and Automation Letters*, vol. 5, no. 2, pp. 3658–3665, 2020.
- [9] M. Sperl, “Experiments on corn pressure in silo cells – translation and comment of janssen’s paper from 1895,” *Granular Matter*, vol. 8, Dec. 2005.
- [10] S. Miyai, M. Kobayakawa, T. Tsuji, and T. Tanaka, “Influence of particle size on vertical plate penetration into dense cohesionless granular materials (large-scale dem simulation using real particle size),” *Granular Matter*, vol. 21, Oct. 2019.
- [11] P. Umbanhowar and D. I. Goldman, “Granular impact and the critical packing state,” *Phys. Rev. E*, vol. 82, p. 010 301, 1 2010.

- [12] F. Qian, T. Zhang, W. Korff, P. B. Umbanhowar, R. J. Full, and D. I. Goldman, “Principles of appendage design in robots and animals determining terradynamic performance on flowable ground,” *Bioinspiration & Biomimetics*, vol. 10, no. 5, p. 056 014, 2015.
- [13] J. Aguilar and D. Goldman, “Robophysical study of jumping dynamics on granular media,” *Nature Physics*, vol. 12, pp. 278–283, 2016.
- [14] P. Holmes, “The dynamics of repeated impacts with a sinusoidally vibrating table,” *Journal of Sound and Vibration*, vol. 84, no. 2, pp. 173–189, 1982.
- [15] D. Wettergreen and C. Thorpe, “Gait generation for legged robots,” in *Proceedings of the IEEE/RSJ International Conference on Intelligent Robots and Systems*, vol. 2, 1992, pp. 1413–1420.
- [16] E. R. Westervelt, J. W. Grizzle, C. Chevallereau, J. H. Choi, and B. Morris, *Feedback control of dynamic bipedal robot locomotion*. CRC press, 2018.
- [17] M. Kelly, “An Introduction to Trajectory Optimization: How to Do Your Own Direct Collocation,” *SIAM Review*, vol. 59, no. 4, pp. 849–904, 2017.